Nano Research

Open Access

Research Article

Ultra-sensitive magnetic nanomechanical array sensor based on graphene oxide for single bacterial cell detection

Zihan Qiao[1,§], Kainan Mei[1,†,§], Yu Wang[1], Tianhao Yan[2], Shubo Zhang[3,4], Qiubo Chen[1], Ye Chen[1], Chen Wang[1], Tianxiang Ren[1], Shangquan Wu[1,5] ✉, and Qingchuan Zhang[1] ✉

[1] *CAS Key Laboratory of Mechanical Behavior and Design of Material, Department of Modern Mechanics, University of Science and Technology of China, Hefei 230027, China*
[2] *Department of Cell Biology and Genetics, College of Basic Medical Sciences, Jilin University, Changchun 130021, China*
[3] *School of Mechanical and Aerospace Engineering, College of Engineering, Nanyang Technological University, Singapore 639798, Singapore*
[4] *Institute of Flexible Electronics Technology of THU, Jiaxing 314000, China*
[5] *State Key Laboratory of Nonlinear Mechanics, Institute of Mechanics, Chinese Academy of Science, Beijing 100190, China*
[†] *Present address: Hefei National Research Center for Physical Sciences at the Microscale, Department of Chemical Physics, University of Science and Technology of China, Hefei 230026, China*
[§] *Zihan Qiao and Kainan Mei contributed equally to this work.*

Cite this article: *Nano Research*, **2025**, *18*, 94907290. https://doi.org/10.26599/NR.2025.94907290

ABSTRACT: Pathogenic bacterial infections pose major health threats and economic burdens. Rapid and highly sensitive biochemical sensors are essential for bacterial detection in food safety and clinical applications. Here, we introduce a graphene oxide (GO)-based magnetic nanomechanical array sensor that utilizes the large surface area of GO to bind more magnetic nanoparticles (MNPs) and aptamers. Rapid and ultra-sensitive detection can be achieved even at extremely low target concentrations. This approach can directly detect a single *Escherichia coli* cell without time-consuming bacterial culture, and the linear detection range is 1–100 CFU·mL^{-1}. Meanwhile, the sensor showed good specificity, reproducibility, stability, and stance to interference, and could detect 1 CFU·mL^{-1} *Escherichia coli* in milk. Moreover, we realized the simultaneous detection of two bacteria at extremely low concentrations, which proved that the sensor had the potential for high-throughput detection. In addition, for extremely low-concentration samples (< 100 CFU·mL^{-1}), we controlled the magnetic force at the tip of the microcantilever, greatly enhancing its deflection and sensitivity. This method provides a novel and ultrasensitive method for the timely detection of pathogenic bacteria, and can also be applied to the highly sensitive detection of other targets such as DNA, small molecules, proteins, and viruses by using different probes. Our research provides a promising tool for effective, rapid and highly sensitive detection in the field of public health and food safety.

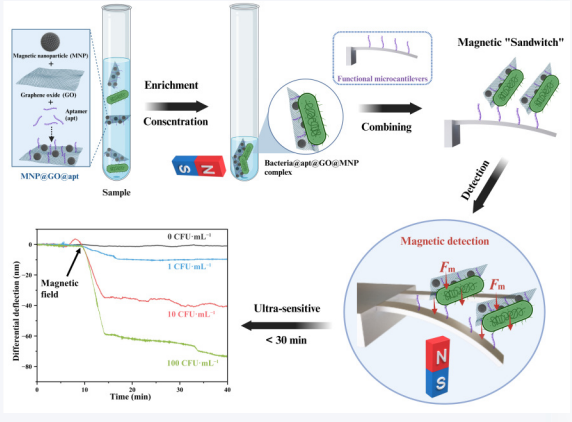

KEYWORDS: bacterial detection, microcantilever array, graphene oxide, magnetic force, nanomechanical sensor

1 Introduction

Controlling food contamination has become increasingly challenging due to the acceleration of globalized food flows. The difficulty in controlling food contamination has resulted in a persistently high incidence of foodborne diseases worldwide, posing a significant public health problem [1]. According to the World Health Organization (WHO), foodborne infections are a major cause of global diseases [2]. Among these, bacteria are the predominant contaminants responsible for foodborne illness. Pathogenic bacteria like *Escherichia coli* (*E. coli*), *Staphylococcus aureus* (*S. aureus*) and *Salmonellosis* are primary culprits, causing illnesses such as food poisoning, hemolytic uremic syndrome, and hemorrhagic enteritis, which are transmitted through contaminated food or water. Even worse, these bacteria can cause even severe and life-threatening diseases, such as cancer and failure of organs [3, 4].

Received: December 10, 2024; **Revised:** January 23, 2025
Accepted: February 6, 2025

✉Address correspondence to Shangquan Wu, wushq@ustc.edu.cn; Qingchuan Zhang, zhangqc@ustc.edu.cn

To reduce these health risks, detecting pathogenic bacteria in the early stages of infection and blocking the spread of their infectious source is crucial. However, in the initial stages of biological contamination, the extremely low concentration of contaminants often goes undetected, misleadingly deeming the food or water safe. Consequently, pathogenic bacteria can enter the body and cause infections through contaminated food and water [5]. Meanwhile, Chinese National Standards require total bacteria counts in natural mineral water to be less than 100 CFU·mL^{-1}, with *E. coli* should be 0 (per 100 mL of water sample) [6]. In addition, with the breakthrough of new cell therapy in cancer treatment, the traditional sterility test method was not sensitive enough to detect less than 1 CFU·mL^{-1}. This poses a great risk to cell therapy, because bacterially contaminated cell therapy drugs may lead to treatment failure, including poor patient prognosis and therapeutic effects [7–9]. It is necessary to take measures to prevent the risk of bacterial infection and the spread of biological pollution to ensure the human health and public safety.

Although the conventional bacterial culture method has high sensitivity in the detection of bacteria, and the detection range can reach 1–1 × 10^4 CFU·mL^{-1}, this method requires several days or even a week to culture the bacteria to a state that can be quantified. Moreover, some pathogenic bacteria, such as *Mycobacterium leprae* and *Rickettsia*, cannot be cultured under the conditions known in the laboratory due to the need for special hosts [10–12]. Quantitative polymerase chain reaction (qPCR) enables the targeted amplification of bacterial DNA sequences into multiple copies for subsequent detection. The bacterial detection limit of qPCR was typically in the range of approximately 1 × 10^3–1 × 10^4 CFU·mL^{-1}, with the detection time generally more than 15 h [13]. Immunological bacterial detection was also commonly used, among which enzyme-linked immunosorbent assays (ELISAs) were the most prevalent. However, the detection limit of this technology is typically in the range of 1 × 10^4–1 × 10^5 CFU·mL^{-1} [14]. These methods fail to meet the rapid and ultra-sensitive pathogenic bacteria detection, and because these methods require a long time to detect, it is difficult to meet the demands of rapid detection of food before deterioration.

In recent years, certain new biosensors exhibited higher detection sensitivity. For instance, the nanoporous gold electrode constructed by Ranjbar et al. can quantitatively detect *Salmonella typhimurium* at 6.5 × 10^2 CFU·mL^{-1}. However, the preparation of the sensing electrode of the sensor is complicated and has long time [15]. Pankratov et al. utilized an electrochemical sensor with cellulase-linked immunomagnetic beads for the detection of *E. coli*, achieving a detection limit of 1 CFU·mL^{-1}. However, this method requires multiple labeling of the target, resulting in complex and time-consuming sample preparation, which requires immunomagnetic bead labeling and antibody/aptamer-enzyme labeling successively [16]. In addition, Kim et al. developed a highly sensitive single-cell bacteria detection method based on super-resolution fluorescence imaging and artificial intelligence (AI) analysis, but the limit of detection (LOD) was 28 CFU·mL^{-1} due to the shedding of the target caused by the washing step. Moreover, super-resolution microscopy and AI image analysis require expensive equipment and expertise, which limits the application of the sensor in practical scenarios such as clinical [17]. In conclusion, there is an urgent need to develop a rapid, effective and highly sensitive pathogen detection method to address the existing issues of current detection methods and meet the pressing demand for detection in various application scenarios.

Microcantilever sensing can detect a target by utilizing a specific binding of probe and target to induce deflection of the microcantilever, which has the advantages of high sensitivity, fast response, and real-time monitoring [18–22]. The tiny deflection of the microcantilever tip is read through an optical lever [23, 24]. We have achieved progress in the highly sensitive detection of novel coronavirus N genes [25] cancer markers [26] and other substances [27] using microcantilever sensing. However, the detection limit of traditional microcantilever sensing based on the change of surface stress for bacteria is only 1 × 10^6 CFU·mL^{-1} [28]. In addition, Sungkanak et al. successfully detected bacteria using a sensor that utilizes the resonant frequency shift of a microcantilever due to the mass changes [29–31] after bacterial binding. The detection limit achieved 1 × 10^3 CFU·mL^{-1} [32]. However, the detection of bacteria at low concentrations (< 1 × 10^3 CFU·mL^{-1}) based on surface stress or mass change was challenging. Therefore, improving the sensitivity of microcantilever sensors is necessary to satisfy the demand for detecting extremely low concentrations of bacteria.

In our previous study on detecting cancer-derived exosomes [33], we developed a new mode of mechanical signal generation using controllable magnetic forces provided by magnetic nanoparticles (MNPs), which significantly enhanced the detection sensitivity. Specifically, microcantilever deflection was caused by the controllable magnetic force provided by MNPs in the magnetic field, rather than by weak intermolecular forces in surface stress mode [34]. This novel mode fundamentally changed the generation of force that deflects the microcantilever. The microcantilever deflection was influenced by both the magnetic force experienced by a single MNP and the number of MNPs that bind to the target. However, in samples with extremely low concentrations, only a few bacteria exist. This results in a limited production of magnetic forces by a small quantity of MNPs when a magnetic field is applied. Therefore, increasing the number of MNPs bound to each target can increase the force acting on each target, which in turn amplifies the microcantilever deflection caused by magnetic force, improving the sensitivity of detecting pathogenic bacteria at extremely low concentrations.

Graphene oxide (GO) is a material formed by the oxidation of graphene, which is a lattice-like material composed of tightly packed carbon atoms. By modifying the surface of GO with functional groups, the biological activity of the GO can be greatly improved, providing applications of GO in biomedicine and biosensors [35–37]. Furthermore, due to its large surface area, GO can be coated on other nanoparticles for the capture and enrichment of peptides or proteins. When GO was used as the coating layer of MNPs, compared with single MNP, GO-coated MNPs increased the specific surface area of single MNP and the number of MNPs acting on the target. This leads to an increase in the magnetic force applied to a single target in the magnetic field. GO also enhanced the superparamagnetic properties of the MNPs [38, 39]. Therefore, GO-coated MNPs are expected to increase the magnetic force acting on individual MNPs in the magnetic field and increase the number of MNPs generating a magnetic force. This would generate a larger magnetic force and further improve the sensitivity of the mechanics-based sensor.

Here, we describe a novel magnetic nanomechanical biosensor based on GO-coupled MNPs. We used specific aptamers as capture and recognition probes for bacteria, and two magnetic composites were synthesized and characterized accordingly. Based on this, we tested the traditional stress mode and two magnetic modes to

compare the sensitivity of different detection modes. We further found the impact of the position change of the magnetic force on the signal generated by the sensor, and explored the relationship with the bacterial detection concentration. Meanwhile, we tested the performance of the sensor, including specificity, anti-interference, reproducibility and stability. In addition, we tested the applicability of the sensor by detecting bacteria in milk samples, and we also performed simultaneous detection of two bacteria, tapping the potential of the sensor to achieve high-throughput detection. As a conceptual verification, we selected the common pathogenic bacteria *Escherichia coli* DH5α as the model bacteria as the detection target, and the detection process is shown in Fig. 1.

2 Results and discussion

2.1 Characterization of bacteria

The *E. coli* DH5α samples with known concentrations (2.36×10^7 and 1.363×10^9 CFU·mL^{-1}) were obtained through bacterial proliferation culture and plate counting (details were in the Electronic Supplementary Material (ESM)), and the *E. coli* DH5α detection concentration in the experiment was further determined by gradient dilution. The *E. coli* DH5α samples were stained using Gram staining (details are in the ESM), and the results were negative, consistent with *E. coli* being a Gram-negative bacterium (Fig. S1(c) in the ESM). Further, morphological images of *E. coli* DH5α obtained by scanning electron microscope (SEM) (Fig. S1(d) in the ESM) clearly showed that the bacteria in the samples conformed to the general shape and size of *E. coli* (0.5–3 μm).

2.2 Fabrication and characterization of MNP@apt and MNP@GO@apt composites

The aminated MNPs and carboxylated GO form MNP@GO composite through amide bond formation. The membrane protein of *E. coli* DH5α can be specifically recognized by the *E. coli* specific

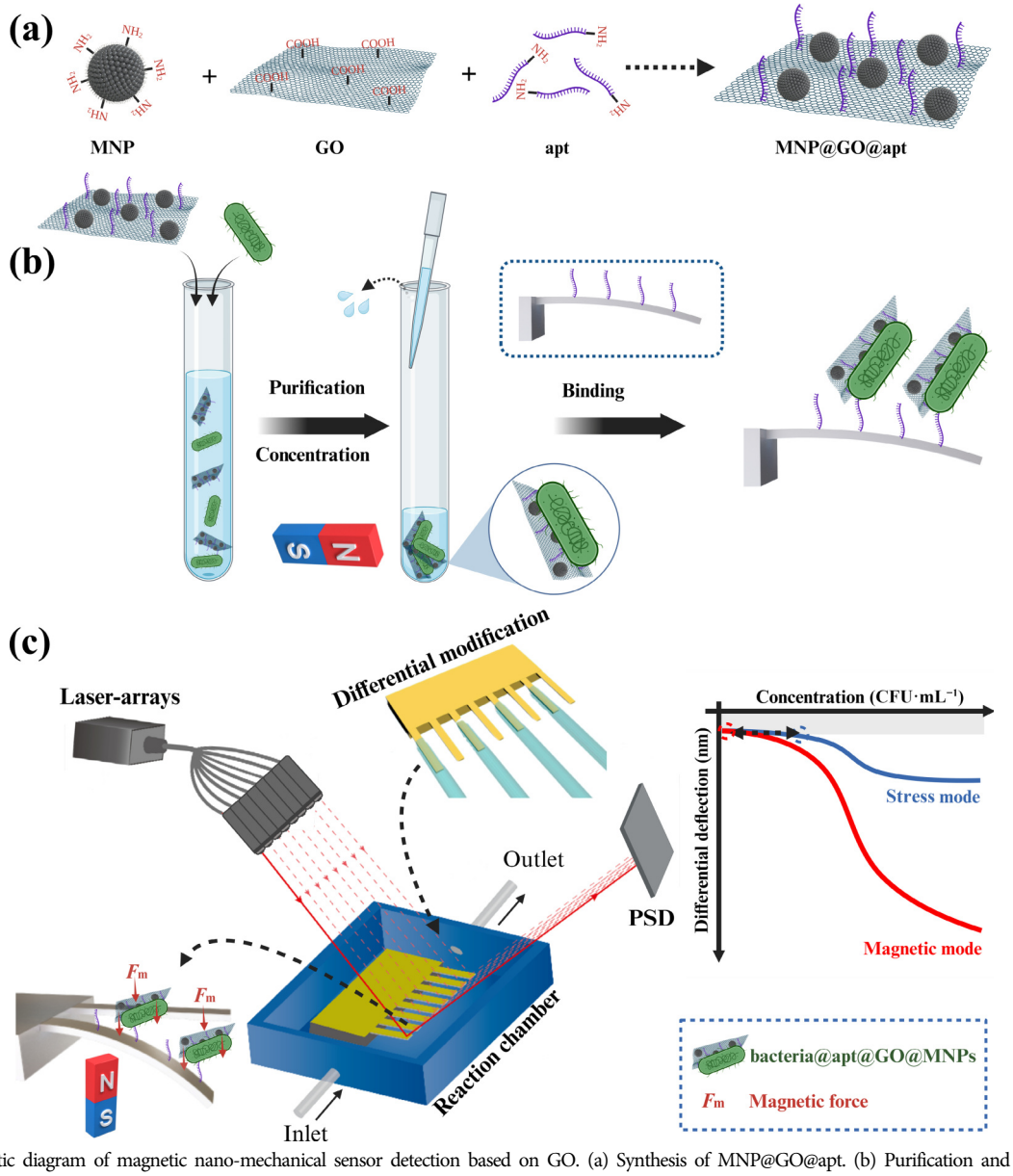

Figure 1 Schematic diagram of magnetic nano-mechanical sensor detection based on GO. (a) Synthesis of MNP@GO@apt. (b) Purification and concentration of bacteria, binding to microcantilevers. (c) GO-coupled MNPs increase the deflection of the microcantilever array in the magnetic field.

aptamer [16]. Subsequently, aminated aptamers are conjugated to the carboxylated GO surface by amide bonds, forming the MNP@GO@apt composite. (Fig. 1(a), details in the ESM), which is a crucial step in the experimental design. The aptamers on the surface of the composite (MNP@GO@apt) can capture bacteria so that under the action of a magnetic field, bacteria, and their complexes (bacteria@apt@GO@MNPs) are enriched at the bottom of the solution (Fig. 1(b)). Due to the large specific surface area of GO, it can encapsulate multiple MNPs on its surface and enhance the efficiency of aptamer coupling. Consequently, the composite increases the magnetic force exerted on individual bacteria, thereby improving the efficiency of bacterial capture. Meanwhile, to validate the effect of the introduced GO on enhancing sensitivity, we used materials only containing MNPs without GO (MNP@apt) as a control experiment. The MNP@apt composite was formed by directly modifying aptamers on the surface of MNPs (details are in the ESM). We designed the following experiments to verify the synthesis of the MNP@apt and MNP@GO@apt composites.

The SEM image (Fig. 2(a)) showed a sheet-like folded structure of GO with a certain level of transparency and displayed a smooth and neat surface. As shown in TEM images, MNPs (approximately 250 nm) exhibited uniform dispersion (Fig. S2(a) in the ESM), and the MNP@GO complex was formed after further coating with GO (Fig. S2(b) in the ESM). Multiple MNPs are present on the surface of GO. After the aptamer was coupled with MNP@GO, the MNP@GO@apt composite was shown in Fig. 2(b). Similarly, after the aptamer was coupled with MNPs, the TEM image of the MNP@apt composite is shown in Fig. 2(c).

Dynamic light scattering (DLS) was used to measure MNP size distribution in a suspension by analyzing the scattering of light caused by their Brownian motion. The DLS results showed that the average hydrodynamic size of the MNPs was approximately 266.3 nm, which increased to 753.1 nm after being coated with GO (Fig. 2(d)). This indicates that a larger size structure (MNP@GO) is formed due to the large surface area of GO and the combination of MNPs, resulting in a significant increase in the particle size of MNP@GO. This suggests that GO was effectively enveloped on the surface of the MNPs. After aptamer conjugation, the mean hydrodynamic size of the complex (MNP@GO@apt) further increased from 753.1 to 773.4 nm (Fig. 2(d)). The difference just matched the size of the aptamer (approximately 23 nm), indicating that the aptamer was successfully coupled to the composite. The polydispersity index (PI) of MNPs, MNP@GO, and MNP@GO@apt were 0.7059, 7.429, and 13.26, respectively, indicating that the lamellar structure of GO caused MNPs to become more clustered and wrapped together (the smaller the PI

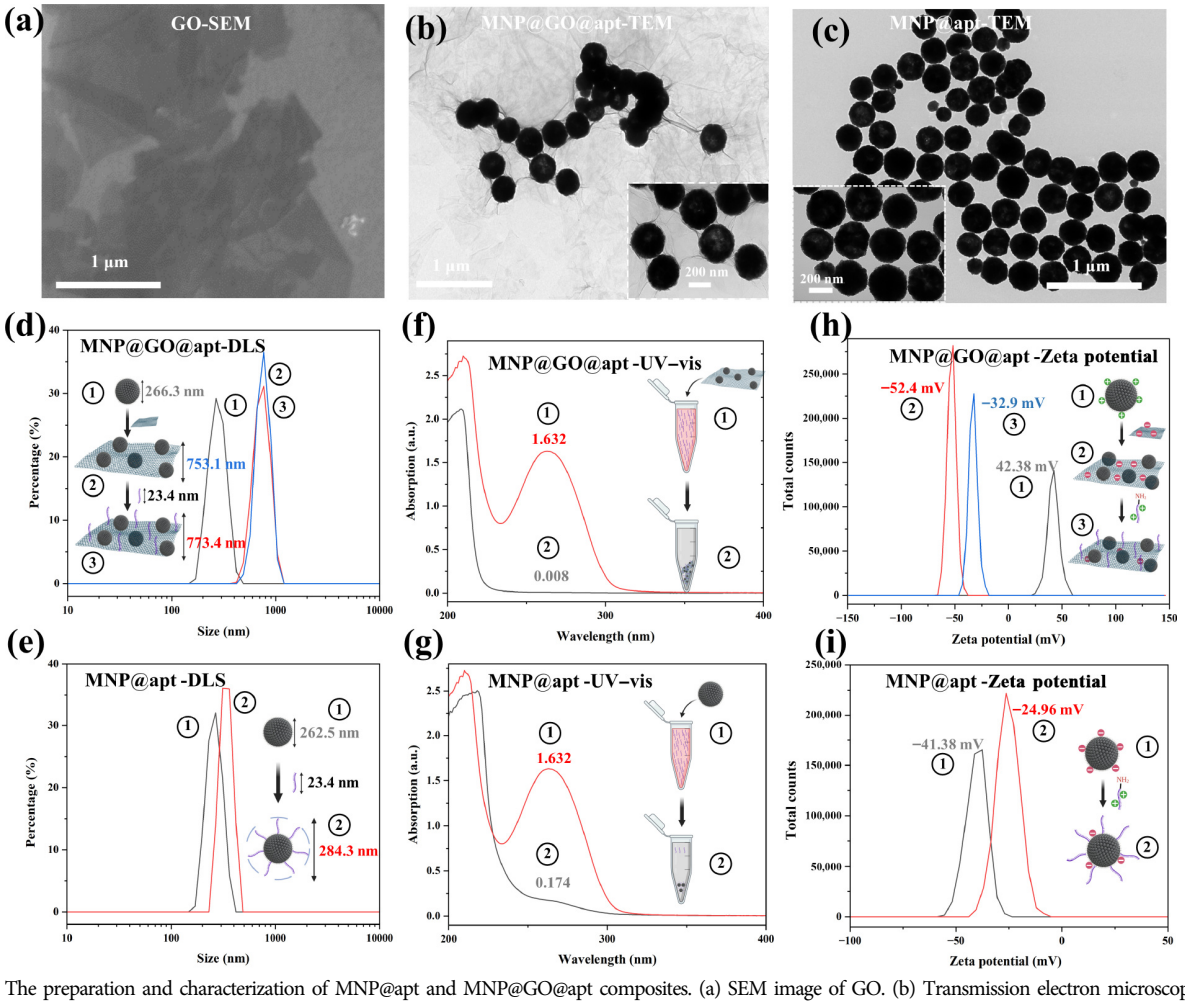

Figure 2 The preparation and characterization of MNP@apt and MNP@GO@apt composites. (a) SEM image of GO. (b) Transmission electron microscope (TEM) image of MNP@GO@apt. (c) TEM image of MNP@apt. (d) DLS of the MNPs, MNP@GO, and MNP@GO@apt. (e) DLS of MNPs and MNP@apt. (g) UV–vis spectroscopy results before and after MNP@GO coupled with aptamers. (f) UV–vis results before and after MNPs coupled with aptamers. (h) Zeta potentials of the MNPs, MNP@GO, and MNP@GO@apt. (i) Zeta potentials of the MNPs and MNP@apt.

value, the better the dispersion of the particles [40]). Similarly, the average hydrodynamic sizes of MNPs after conjugation were 262.5 and 284.3 nm, respectively (Fig. 2(e)), and the PI of MNPs was 0.7063, while the PI of MNP@apt was 0.5791. The DLS results showed that aptamers were successfully coupled to the surface of MNPs to form a well-dispersed MNP@apt. Overall, these results indicate that aptamers are successfully coupled to the surface of MNP@GO to form MNP@GO@apt. At the same time, GO was coated on the surface of MNPs, which increased the surface area of MNPs and the number of MNPs.

To determine the efficiency of aptamer coupling, ultraviolet-visible spectroscopy (UV–vis) was employed to detect the consumption of aptamers in suspension. Specifically, the full-wavelength UV absorption spectra of the supernatant were measured before and after aptamers coupling, within the range of 190 to 800 nm. The absorption of the free aptamer solution before coupling was 1.632 at 263 nm, while the absorption of the supernatant after MNP@GO coupling was significantly reduced to 0.008 at 263 nm (Fig. 2(f)). Therefore, the calculated coupling percentage of the aptamers to MNP@GO was 99.5%. This result shows that the free aptamer in the solution is greatly reduced, indicating that aptamers were successfully modified on the surface of MNP@GO. Similarly, after the aptamer was coupled with MNPs, the absorption of the aptamers at 263 nm was significantly reduced to 0.174 (Fig. 2(g)), indicating that the aptamer was coupled to the surface of MNPs. However, the coupling efficiency of aptamers to MNPs was calculated to be 89.3%. UV–vis results indicated that the aptamer was successfully modified on the surfaces of MNPs and MNP@GO composite. More importantly, the coupling efficiency of GO was higher than that of MNPs, and almost all the free aptamer in the solution was coupled to the surface of MNP@GO. Therefore, the GO coating greatly improved the coupling efficiency of aptamers to better capture bacteria.

The surface Zeta potential explains the surface charge characteristics and stability of the particles by measuring the electric potential of the particles when they move in the suspended electric field. The Zeta potential results showed that the initial Zeta potential of the MNPs was 42.38 mV after amidation and changed to −52.4 mV after being coated with GO (Fig. 2(h)). This is consistent with the fact that GO carries an enormous negative charge, which leads to the negative charge of the MNP@GO@apt composite. After being coupled with aptamers, the Zeta potential of MNP@GO was −32.9 mV. The potential change occurred because the aptamer with amino groups became positively charged in an acidic solution, which neutralized part of the negative charge on the surface of MNP@GO. Likewise, the Zeta potentials of the MNPs and MNP@apt were −41.08 and −24.96 mV, respectively (Fig. 2(i)). Here, the aptamer with the amino group was positively charged, and the MNPs with the carboxyl group were negatively charged. Therefore, when the aptamer was coupled to the MNPs in an acidic solution, the negative charge of MNP@apt was reduced. These results indicated that MNP@apt and MNP@GO@apt composites were successfully prepared and that the aptamer was successfully conjugated with both MNPs and MNP@GO.

2.3 Enhanced bacterial capture by MNP@GO@apt

As shown in Fig. 1(b), *E. coli* in solution was initially captured by MNP@GO@apt and subsequently enriched, purified, and concentrated under the magnetic field. The bacteria then bind to aptamers which were immobilized on the microcantilever surface, forming a "magnetic sandwich" structure. This structure causes the microcantilever to deflect due to the magnetic force generated by the MNPs. Therefore, the capture of bacteria is crucial for the formation of the bacteria@composite complex. To directly verify the binding of bacteria to MNP@GO@apt, *E. coli* DH5*α* was mixed with MNP@GO@apt and enriched, purified, and concentrated. Then the MNP@ GO@apt composite without capturing bacteria was washed and bacteria@composite was prepared. SEM images showed that 1×10^4 CFU·mL^{-1} *E. coli* was bound with multiple MNPs coated by GO and the surface of several bacteria around the MNPs was coated with a wrinkled membrane (Fig. S2(e) in the ESM). This indicates that bacteria can be effectively captured by aptamers modified on the GO surface. Similarly, the SEM image of the binding of MNP@apt to *E. coli* was shown in Fig. S2(f) in the ESM, indicating that the bacteria were successfully captured by MNP@apt through aptamers modified on the MNP surface.

2.4 Traditional stress mode for bacteria detection

To investigate the ability of the microcantilever to detect bacteria, we first need to test its response in standard samples (*E. coli* in PBS solution) using the stress mode. This method was based on the generation of intermolecular forces that cause the microcantilever deflection (Fig. S3(a) in the ESM). During the determination, the sample was directly added to the reaction chamber. We used a capillary to infiltrate the microcantilever into the aptamer solution by a differential modification device to achieve *in situ* control of the experimental microcantilevers and the reference microcantilevers (Fig. S3(b) in the ESM). The aptamer, which specifically captures *E. coli* DH5*α*, was immobilized on the surface of the experimental microcantilevers Nos. 1, 3, 5, and 7. In contrast, microcantilevers Nos. 2, 4, 6, and 8 were only blocked with 6-mercapto-1-hexanol (MCH) as control microcantilevers (Fig. 3(a)). The deflection of the experimental and control microcantilever was averaged, and the average value of the two was subtracted to obtain the differential deflection (Fig. 3(b)). Due to the continuous binding of *E. coli* to the aptamer, the deflection of the microcantilever gradually increased to the maximum with time (Fig. S3(c) in the ESM).

With the concentration of bacteria constantly decreasing, microcantilevers also showed a decreasing differential deflection. When different concentrations of *E. coli* samples of 1×10^8, 1×10^7, and 1×10^6 CFU·mL^{-1} were used in the detection, the corresponding differential deflections were measured as 254, 42, and 8 nm within 60 min, respectively (Fig. 3(c)). Especially at 1×10^6 CFU·mL^{-1}, there was quite tiny. Therefore, the detection limit of *E. coli* DH5*α* using the stress mode could only be 1×10^6 CFU·mL^{-1}. This result is comparable to the stress mode reported previously [28]. However, achieving low-concentration bacterial detection in the early stage of food contamination by stress mode detection was difficult.

2.5 Magnetic force mode based on MNPs

To further improve the detection limit for bacteria, we used the magnetic mode based on MNP@apt to detect *E. coli* DH5*α* (details are in the ESM). The synthesized MNP composite was used to capture *E. coli*. After enrichment by magnetic force (Fig. S5(a) in the ESM), the *E. coli*@apt@MNPs complex was captured by aptamers on the microcantilever surface to form a "magnetic sandwich" structure. Finally, the microcantilever was placed in a magnetic field, and MNPs generate magnetic force to deflect the microcantilever (Fig. S5(b) in the ESM). The simulation results in

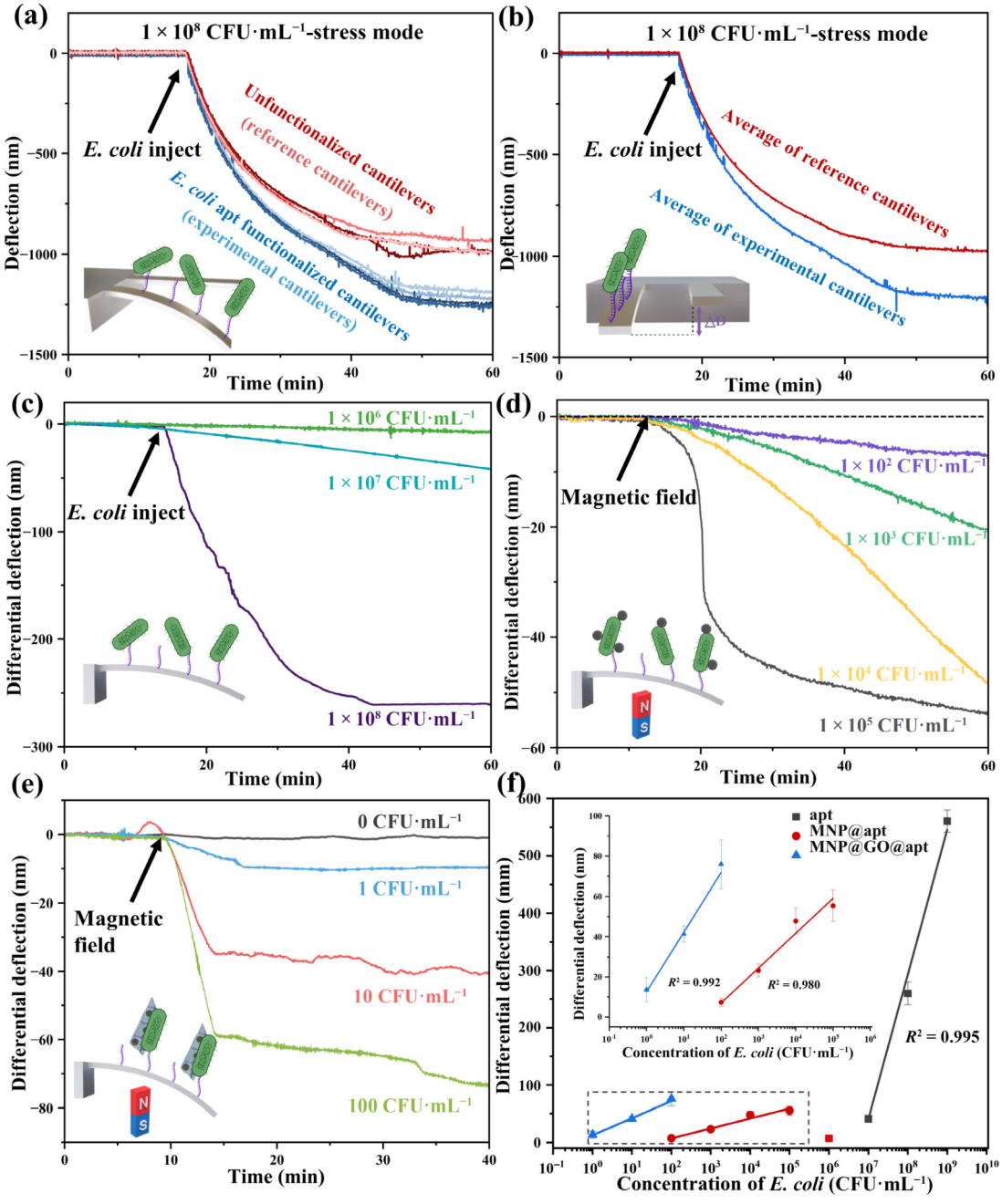

Figure 3 Results of the detection of *E. coli* with stress mode and two magnetic detection modes. (a) *In situ* comparison of microcantilevers array. A significant differential deflection between functionalized (experimental, red line) and non-functionalized (reference, blue line) microcantilevers was observed when 1×10^8 CFU·mL^{-1} *E. coli* was injected. (b) The average values of the experimental and reference microcantilevers in (a). (c) Traditional stress mode detection of *E. coli*. (d) Magnetic detection results using MNP@apt for *E. coli*. (e) Magnetic detection results using MNP@GO@apt for *E. coli*. (f) Linear fitting of the sensitivity of three microcantilever sensors for detecting *E. coli* ($n = 3$, bars represent mean ± SD).

Figs. S6 and S7 in the ESM show the magnetic fields used in this experiment. The detection results indicated that the concentrations of bacteria at 1×10^5, 1×10^4, 1×10^3, and 1×10^2 CFU·mL^{-1} caused differential deflections of 54, 48, 20, and 7 nm within 60 min, respectively (Fig. 3(d)). Compared to the stress mode, the magnetic mode based on MNP has a detection limit of 1×10^2 CFU·mL^{-1} for *E. coli* in the mechanical enhancement method, and the performance is improved by 4 orders of magnitude. This indicates that the introduction of magnetic force makes the surface of the microcantilever produce a greater force change than the intermolecular force, in order to obtain the highly sensitive detection results. However, it still does not meet the detection requirements for certain scenes of bacteria (1 CFU·mL^{-1} or less).

2.6 Magnetic force mode based on GO-coupled MNPs composite

The microcantilever deflection was influenced by the magnetic force from MNPs binding to the target. In samples with low bacterial concentrations, few MNPs generate magnetic force. To address this, we utilized GO for its large surface area, which can couple more MNPs, increasing the magnetic force on each target

and amplifying the deflection. Additionally, GO allows for more aptamers to capture the target and enhances the paramagnetism of MNPs, ensuring sufficient magnetic force from individual MNPs. Like MNP, *E. coli* was captured by specific aptamers modified on GO. After magnetic enrichment, purification, and concentration, the bacterial complex (bacteria@apt@GO@MNPs) bound to the aptamers on the surface of the microcantilever to form a "magnetic sandwich" structure. To ensure a fair comparison of sensitivity, the concentration of MNP@GO@apt used was identical to that of MNP@apt, and the aptamer concentration employed as the probe molecule was also the same. The *in situ* control (experimental and reference cantilevers) was formed by differential modification of aptamers on the surface of the microcantilever array ("Differential modification" in Fig. 1(c)). Finally, the microcantilever array was placed in the reaction chamber without liquid flow and the microcantilever exhibited significant deflection under magnetic force. This instantaneous deflection change is detected by eight parallel lasers.

The results showed in Fig. 3(e), when the bacterial concentration was 100 and 10 CFU·mL^{-1}, the differential deflection was significant at 74 and 43 nm within 40 min, respectively. Moreover, when the bacterial concentration was only 1 CFU·mL^{-1}, a differential deflection of 8 nm was still detected. These results show that compared with MNPs-based microcantilever biochemical sensing, the sensitivity of MNP@GO in bacterial detection is further improved. This method can still identify *E. coli* with very high sensitivity for 1 CFU·mL^{-1} in the sample. Meanwhile, from the curve in Fig. 3(e), we infer that when the bacterial concentration is high, the number of GO-coupled MNPs composite is also high, which may cause the microcantilever to be pulled down by a large magnetic force. Even if the bacterial concentration is reduced, the GO-coupled MNPs composite can produce a significant deflection and complete the detection within 40 min. This indicates that microcantilever biochemical sensing can achieve ultra-sensitive and rapid detection of extremely low-concentration bacterial samples, which can be used in some scenarios that were difficult to detect in the past.

To compare the direct detection results based on surface stress modes with those of two magnetic modes, we plotted and linear fitted the detection results of *E. coli* with different concentrations using the three methods. The LOD is defined as three times the background noise, and the noise of the three detection modes is between 1 and 2 nm. As shown in Fig. 3(f), based on a three-fold noise signal-to noise ratio, the grey line (signal/noise (S/N) = 6) indicates that the LOD of the traditional stress mode was 1×10^6 CFU·mL^{-1}, while the LOD of the magnetic mode based on MNP was reduced to 100 CFU·mL^{-1} (red line, S/N = 4.5). The LOD of the magnetic mode based on GO-coupled MNPs for *E. coli* was reduced to 1 CFU·mL^{-1} (blue line, S/N = 3). The linear detection range of the magnetic nanomechanical sensing method for detecting *E. coli* based on MNP@GO@apt is 1–100 CFU·mL^{-1} and based on MNP@apt is 1×10^2–1×10^5 CFU·mL^{-1}.

In traditional stress mode, impurities in complex samples significantly interfere with the microcantilever's performance. Firstly, impurities in the sample can affect the refractive index and scattering of the solution in the reaction chamber, thereby altering the detection optical path. This results in changes to the optical lever or prevents the light spot from accurately focusing on the tip of the microcantilever, leading to inaccurate results or unsuccessful detection. Secondly, due to the inherent material properties of the microcantilever and its high length-to-thickness ratio, it is extremely flexible and sensitive to disturbances. Consequently, during the continuous introduction of samples into the reaction chamber, the fluid flow and impurities in the sample cause substantial perturbations to the deflection signal, resulting in significant background noise. This makes the stress mode challenging to detect differential signals when the target concentration is low.

However, detection based on magnetic mode can avoid these problems. The impurity interference in the sample is removed by enrichment, purification, and concentration. Meanwhile, the magnetic field can be directly applied under the condition that the liquid (PBS) in the reaction cell is stationary without passing through the sample. Therefore, this mode minimizes the interference caused by liquid flow and impurities in the sample. Additionally, the magnetic force detection mode significantly reduces the time required for the cantilever to reach a steady state by completing the binding of target molecules and probes during the enrichment and purification steps outside the reaction chamber. Optimizations such as increasing the magnetic field strength and gradient, and improving washing protocols to reduce nonspecific adsorption, could further enhance detection efficiency and shorten the detection time.

2.7 Impact of magnetic force position on deflections

Although the extremely low concentration of *E. coli* (1 CFU·mL^{-1}) in the standard sample was successfully detected using GO-coupled MNPs, the differential deflection was only 8 nm (background noise 1–2 nm). However, the position of the bacterial complex (bacteria@apt@GO@MNPs) bound to the surface of the microcantilever through the probe (apt) was random. Therefore, when the bacterial concentration was extremely low (only a single bacterial cell), the bacterial complex was captured at any position on the surface of the microcantilever, thereby generating magnetic force at random positions. According to the principle of material mechanics, the microcantilever deflection is different due to the concentrated force applied at different positions on the surface of the microcantilever. The force applied on the tip of the microcantilever leads to the maximum deflection, and the force applied on the root of the microcantilever leads to the minimum deflection (Fig. 4(a)). Consequently, if the bacterial complex binds to the probe at the root of the microcantilever, the microcantilever deflection caused by the magnetic force will be minimal, which could be less than three times the noise signal. This is difficult to accurately detect the extremely low concentrations of bacteria. However, if the bacterial complex is captured at the tip of the microcantilever, the microcantilever deflection caused by the magnetic force will be significantly larger, enabling the accurate detection of 1 CFU·mL^{-1} of bacteria.

Therefore, we propose modifying the probe at different positions on the microcantilever to control the capture location of the bacterial complex, thereby controlling the position of the generated magnetic force. By differential modification device (Fig. S3(b) in the ESM), we realize the modification of the probe at different positions of the microcantilever, including the modifications of the tip, mid, root, and all on the surface of the microcantilever (Fig. 4(b)). Moreover, the previous experimental results were carried out under the condition that the probe ("All" in Fig. S8(b) in the ESM) was modified on the surface of the whole microcantilever.

The deflection of the microcantilever under a uniform load is calculated using the material mechanics equation (Eq. (1)).

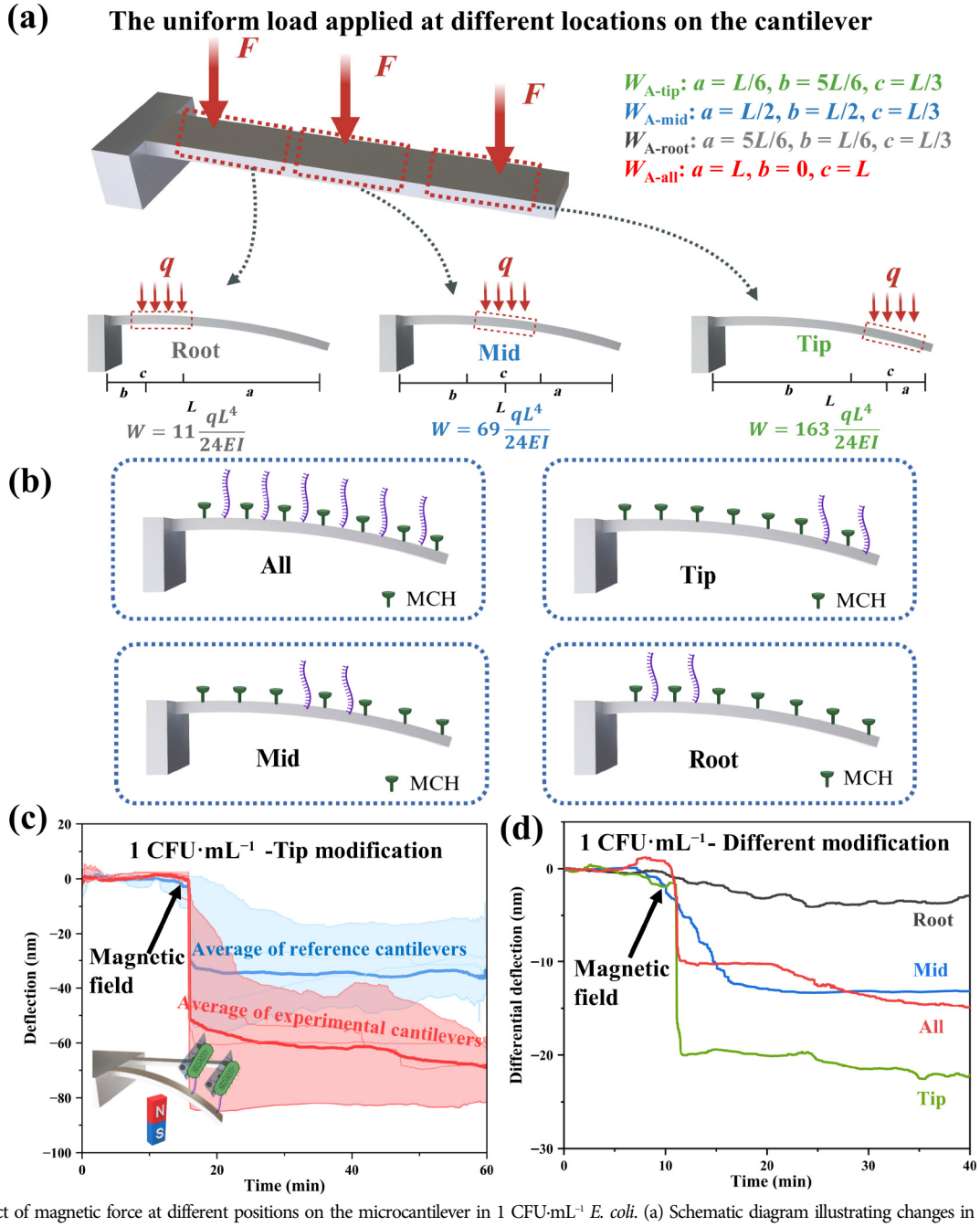

Figure 4 Impact of magnetic force at different positions on the microcantilever in 1 CFU·mL^{-1} *E. coli*. (a) Schematic diagram illustrating changes in deflection due to magnetic force at different positions on the microcantilever. (b) Schematic diagram of the probes at different positions modified on the microcantilever. (c) *In situ* deflection results for tip-modified aptamers in the assay of 1 CFU·mL^{-1} *E. coli*. The red and blue shaded areas represent the deflection ranges of experimental and reference cantilevers, respectively, with thick lines showing the averaged deflection and thin lines indicating real-time deflection of individual cantilevers. A significant differential deflection was observed under the magnetic field. (d) The results of aptamers modified at different positions showed different deflections for 1 CFU·mL^{-1} *E. coli*.

$$W = \frac{qc}{24EI}\left(12b^2L - 4b^3 + ac^2\right) \quad (1)$$

where W is the deflection of the cantilever; q is a uniform load applied to the cantilever; E is the elastic modulus of the cantilever; I is the section inertia moment of the cantilever; L is the length of the cantilever; a, b are the position parameters on the cantilever; c is the length of the uniform load. In Eq. (1), $(12b^2L - 4b^3 + ac^2)$ is the coefficient term, which is used to consider the influence of the position of the applied force on the deflection of the cantilever.

To facilitate the operation of probe differential modification, we divided the modification area on the microcantilever into three parts, one-third of the tip (Fig. S8(a) in the ESM), one-third of the middle (Fig. S8(c) in the ESM), and one-third of the root (Fig. S8(d) in the ESM). Based on the above formula, it can be calculated that when the magnetic force is applied to the tip 1/3 of the microcantilever, the deflection of the microcantilever is the largest, which is 14.8 times of that applied to the root 1/3 of the microcantilever, 2.36 times of that applied to the middle 1/3 of the microcantilever, and 2 times of that applied to the all-modified microcantilever with the probe.

Further, we verified the theoretical inference through experiments. Here, we used the same magnetic detection

experimental method, but the position of the magnetic force was different. After the tip-modified microcantilever was bound to the 1 CFU·mL^{-1} *E. coli* standard sample to form a "magnetic sandwich" structure, the microcantilever rapidly deflected under a magnetic field, exhibiting a differential deflection of 22 nm within 5 min (Fig. 4(c)). In Fig. 4(c), the red shaded area represents the deflection range of the functionalized microcantilevers (experimental group), with thin red lines showing the real-time deflection of individual cantilevers and the thick red line indicating the averaged deflection. Similarly, the blue shaded area represents the deflection range of the non-functionalized microcantilevers (reference group), with thin blue lines indicating the individual deflection and the thick blue line showing the averaged deflection. Meanwhile, we modified the microcantilever array at three other different positions: the mid, the root, and the all. The differential deflection of the microcantilever was 13, 3, and 15 nm, respectively (the "blue", "gray", and "red" lines in Fig. 4(d)). The variation trend of the differential deflection is consistent with the theoretical calculation results. The deflection of the tip-modified microcantilever is the largest, and the deflection of the root-modified microcantilever is the smallest. This result shows that bacteria are captured at the tip of the microcantilever by the probe, thereby controlling the magnetic force at the tip of the microcantilever, and ultimately increases the deflection of the microcantilever, making the bacteria easier to detect.

When the concentration of *E. coli* DH5*α* was further increased to 10 and 100 CFU·mL^{-1}, the differential deflections of the tip-modified microcantilever were 56 and 68 nm (Fig. 5(e)), respectively. Meanwhile, the all-modified microcantilever arrays showed a deflection of 40 and 70 nm (Fig. 5(f)), respectively. These findings show that at a concentration of 100 CFU·mL^{-1}, the differential deflection generated by the microcantilever with the tip-modified probe was comparable to the microcantilever with the all-modified probe. Subsequently, a concentration of 1×10^3 CFU·mL^{-1} of *E. coli* DH5*α* standard sample was used for detection using both tip-modified and all-modified microcantilever, resulting in differential deflections of 60 and 85 nm, respectively (Fig. 5(b)). However, at the concentration of 1×10^3 CFU·mL^{-1}, the deflection of the all-modified microcantilever by the probe was larger than that of the tip-modified microcantilever by the probe. This is because the probe density of the all-modified microcantilever is the same as that of the tip-modified microcantilever. When the bacterial concentration is high, compared to the tip-modified microcantilever, all-modified microcantilever has additional probes in the middle and root that can further capture more bacteria. As a result, compared to the microcantilever that is modified only at the tip with probe, the all-modified microcantilever can bind more bacterial complexes, resulting in greater magnetic force to make the microcantilever deflect larger (Fig. 5(a)). For comparison, at extremely low bacterial concentrations, bacterial complexes may be trapped at any position on the surface of the all-modified microcantilever. This binding may be at the root, middle, or tip of the microcantilever, and the resulting magnetic force is smaller than that of the bacterial complex all bound to the tip (Figs. 5(c) and 5(d)). Therefore, these results indicate that the all-modified microcantilever with the probe can be used for magnetic detection based on MNPs@GO@apt in the case of high bacterial concentration. On the contrary, at low bacterial concentrations, the microcantilever with only a tip-modified probe achieves a greater signal response, making the MNPs@GO@apt magnetic method more sensitive.

To verify whether *E. coli* at extremely low concentrations can truly be captured by the modified probe at the tip of the microcantilever, we used SEM for observation. Figures 6(c) and 6(d) show the results of the experimental cantilever and the reference cantilever in the tip-modified microcantilever array at a concentration of 10 CFU·mL^{-1} *E. coli* DH5*α*. We found that MNP@GO composites were distributed at the tips of the experimental and reference microcantilevers. This result indicated that the MNP@GO composite has a certain non-specific adsorption on the surface of the microcantilever, which leads to a certain deflection of the reference microcantilever under magnetic force. This effect is represented by the blue shaded area in Fig. 4(c), which shows the deflection range of the reference cantilevers. At the same time, this also shows that the method can achieve the enrichment of 1 CFU·mL^{-1} bacteria. Additionally, only two *E. coli* DH5*α* enveloped by MNP@GO@apt were found at the tip of the experimental cantilever, with Figs. 6(a) and 6(b) showing magnified images of these two bacteria. These enlarged images provide a view of the number of MNPs bound to a single *E. coli* bacterium, forming the basis for theoretical calculations of magnetic-driven microcantilever deflection in subsequent experiments.

2.8 Theoretical verification of detecting 1 CFU·mL^{-1} *E. coli*

To theoretically verify the possibility of detecting 1 CFU·mL^{-1} *E. coli* by magnetic mode, the magnetic field simulation and the magnetic force calculation were conducted. Firstly, we established a model of a neodymium magnet (Fig. S6(b) in the ESM) in COMSOL software to simulate the neodymium magnet used in the experiment. We obtained the simulation results of its magnetic field strength and magnetic field gradient (Fig. S7 in the ESM). Then, the magnetic force of a single MNP is calculated according to the magnetic force calculation equation described in the literature [33].

The equation for calculating magnetic force is as follows (Eq. (2)):

$$F = \mu_0 \kappa V H \nabla H = \mu_0 M V \nabla H \quad (2)$$

where κ is the volume magnetization rate of MNPs that M/H can calculate, M is the saturation magnetization strength of MNPs (Fig. S6(a) in the ESM), H is the magnetic field strength (Fig. S7(a) in the ESM), ∇H is the magnetic field gradient (Fig. S7(b) in the ESM), μ_0 is the vacuum permeability, and V is the MNP volume.

It can be seen from Eq. (2) that the magnetic force generated by a single MNP is proportional to the saturation magnetization strength, the particle size of MNPs, and the magnetic field gradient. Here, the particle size of the GO-coupled MNPs used is approximately 250 nm. The 250 nm MNPs have a larger specific surface area than the micron-sized particles, which means that they provide more surface areas for binding to the target molecule at the same mass. Meanwhile, nano-sized particles usually exhibit superparamagnetism, meaning they can be magnetized rapidly under an external magnetic field, but quickly lose magnetism once the magnetic field is removed, reducing magnetic aggregation between particles. However, the micron-sized particles are easy to form permanent magnetization, which leads to particle aggregation and affects the detection results [38, 39, 41]. Further, the magnetic force is proportional to the third power of the diameter. Therefore, we chose MNP with a diameter of about 250 nm instead of smaller MNP such as 10 nm used in our previous studies [33]. In addition, we note that the magnetic field gradient in Eq. (2) is related to the relative position between the microcantilever and the magnetic

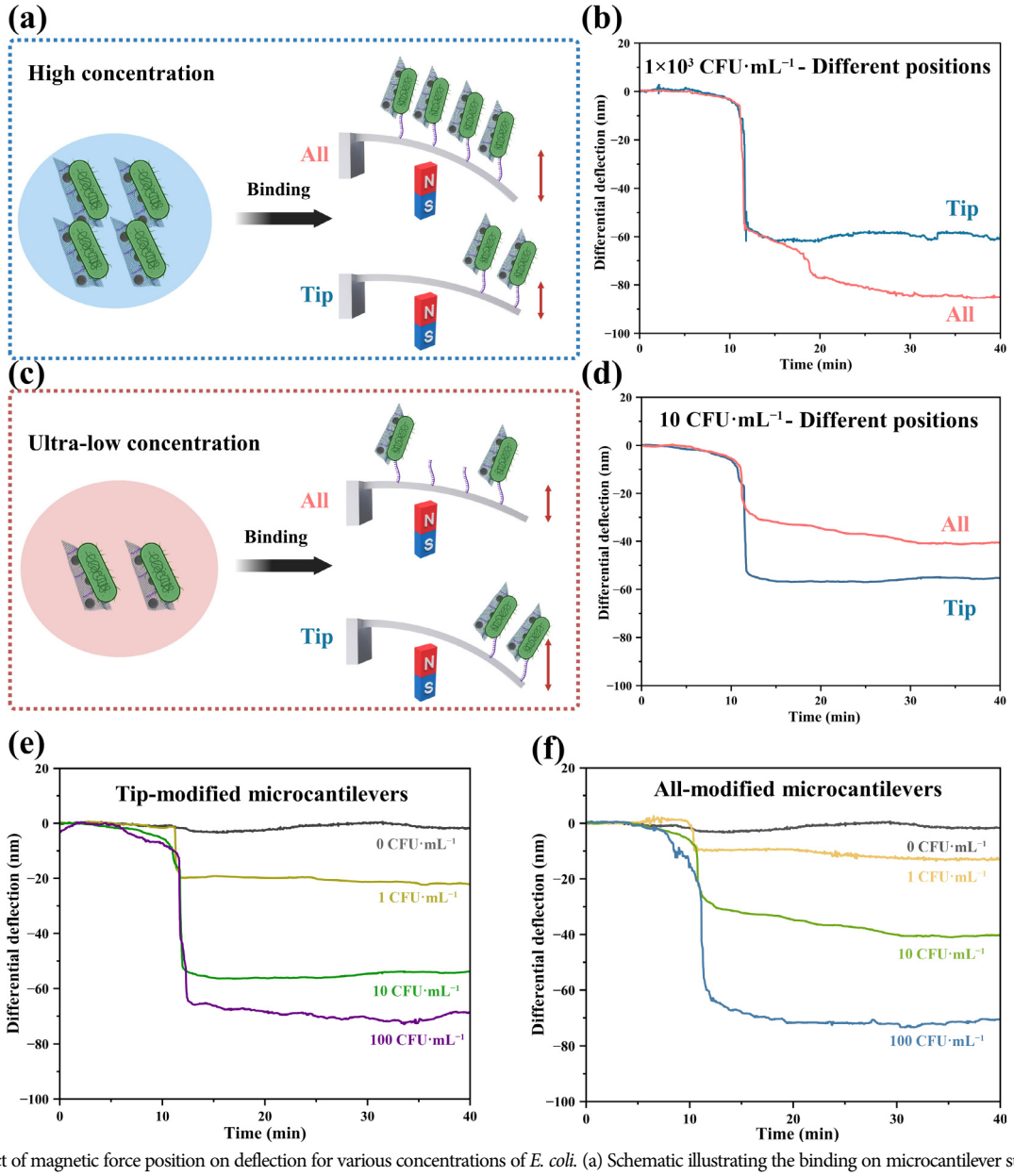

Figure 5 Impact of magnetic force position on deflection for various concentrations of *E. coli*. (a) Schematic illustrating the binding on microcantilever surfaces when the tip or all-modified aptamers detect high concentrations of *E. coli*. (b) Differential deflection plots for tip or all-modified aptamers detecting 1×10^3 CFU·mL^{-1} *E. coli*. (c) Schematic illustrating the binding on microcantilever surfaces when the tip or all-modified aptamers detect extremely low concentrations of *E. coli*. (d) Differential deflection plots for the tip or all-modified aptamer assay detecting 10 CFU·mL^{-1} *E. coli*. (e) Differential deflection plots for tip-modified microcantilever of low and extremely low concentrations of *E. coli*. (f) Differential deflection curves for all-modified microcantilever of low and extremely low concentrations of *E. coli*.

field. As shown in the simulation results of the magnetic field gradient, the closer to the top of the magnet, the greater the magnetic field gradient ("×" position in Fig. S7(b) in the ESM).

Therefore, optimizing the magnetic field device and changing this distance can change the magnetic field intensity and gradient to affect the magnetic force generated by a single MNP. This means that under the same experimental conditions, the deflection of the microcantilever can be increased by changing the distance for the application of the magnetic field. To achieve this, we positioned the magnetic field as close to the microcantilever as possible to generate a greater magnetic force on the MNPs. Consequently, using Eq. (2), the magnetic force of a single MNP is calculated to be about 3.5 pN, and the calculation parameters are shown in Table S1 in the ESM. When detecting 1 CFU·mL^{-1} *E. coli*, the magnetic force applied to the microcantilever is used as a concentrated force. The size of the microcantilever is 500 μm long, 90 μm wide and 1 μm thick. According to the results of SEM (Figs. 6(c) and 6(d)), we estimated that a single *E. coli* carried 13 MNPs, so the maximum microcantilever deflection in detecting a single bacterium was calculated to be approximately 25 nm based on Eq. (1).

2.9 Performance evaluation of the presented sensor

To verify the specificity of our method, *S. aureus* and *Salmonella* were selected for detection on our sensor. *E. coli* is one of the primary causative agents of foodborne illness. *S. aureus* is known to cause foodborne illness and is reported by the Centers for Disease Control and Prevention in USA (CDC) to be the second most infectious bacterium after *E. coli*. *Salmonella* is the main cause of

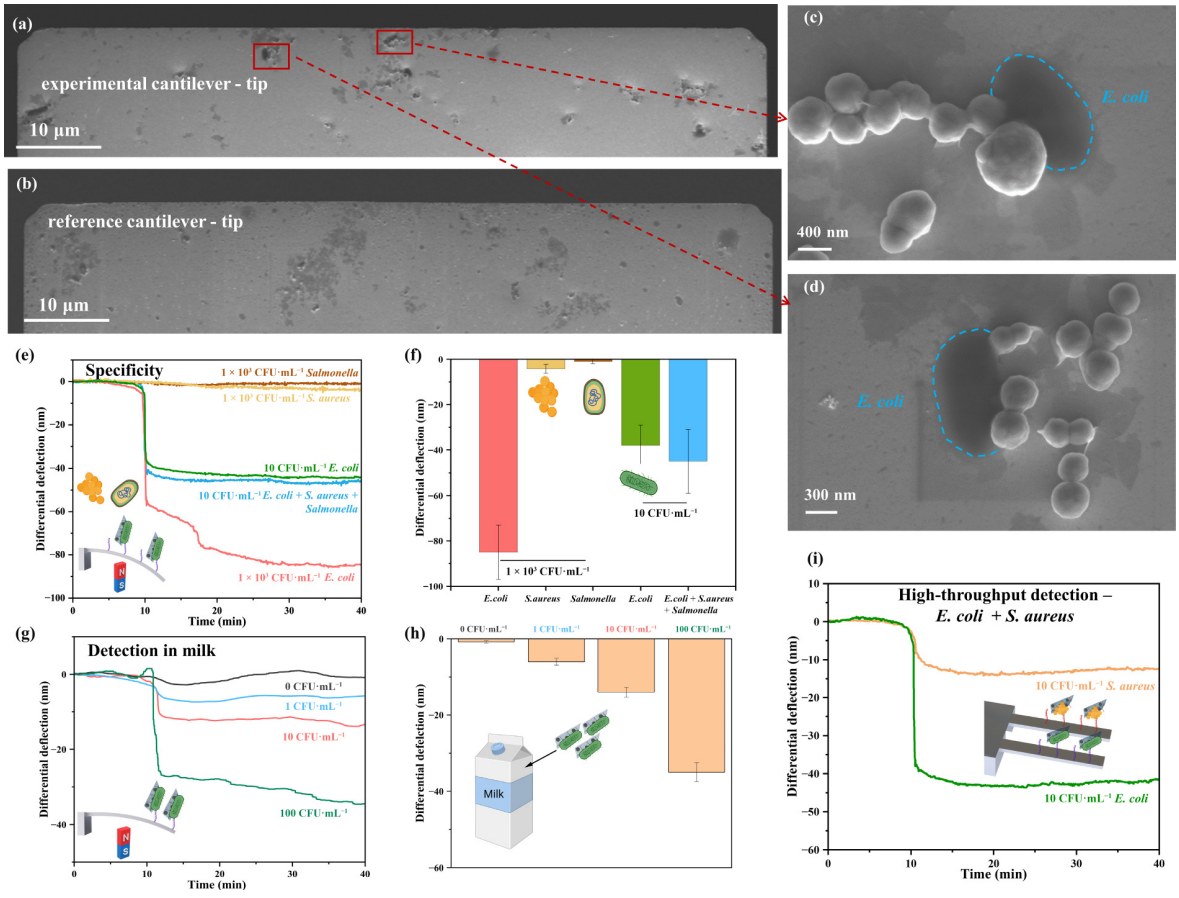

Figure 6 SEM images of the microcantilever tip, selectivity and adaptability of the sensor. (a) SEM image of the tip of experimental microcantilever. (b) SEM image of the tip of reference microcantilever. (c) Magnified view of the red box on the right side of (a). (d) Magnified view of the red box on the left side of (a). (e) Differential deflection curves of specificity and anti-interference detection. (f) Histogram of differential deflections for specificity and anti-interference detection (n = 3, bars represent mean ± SD). (g) Differential deflection curves for detecting different concentrations of *E. coli* in milk. (h) Histogram of differential deflections for detecting different concentrations of *E. coli* in milk (n = 3, bars represent mean ± SD). (i) Differential deflection in high-throughput detection of two bacteria.

human food poisoning, generally due to the consumption of contaminated animal-derived foods (mainly eggs, meat, poultry and milk) [2, 3]. The three foodborne pathogens were detected by the same experimental method, and the detection concentration was 1 × 10^3 CFU·mL^{-1}. Among them, the aptamer we used can specifically recognize the membrane protein on the surface of *E. coli* and is not specific to the other two bacteria [16]. We detected the samples containing *S. aureus* and *Salmonella* respectively. The results in Figs. 6(e) and 6(f) showed that in the magnetic field, the minimal deflections of the microcantilever caused by the detection of *S. aureus* (yellow line, 4 nm) and *Salmonella* (brown line, 1 nm) were significantly smaller than that caused by *E. coli* (redline, 85 nm). Furthermore, we detected the mixed samples of three bacteria (blue line, 45 nm) with a concentration of 10 CFU·mL^{-1}, and the obtained differential deflection was similar to the detection of 10 CFU·mL^{-1} *E. coli* alone (green line, 38 nm), and the difference was within the error range. Therefore, this indicated that our method is only specific to *E. coli*, and has great selectivity and anti-interference performance.

Meanwhile, we also tested the reproducibility and stability of the sensor. For each detection cycle, a new microcantilever array chip was used, eliminating the need to remove the bacteria@apt@GO@MNP complexes bound to the aptamer. The same concentration of *E. coli* (10 CFU·mL^{-1}) was used for detection. Experiments were performed using three parallel microcantilever arrays. The microcantilever array, which combines bacteria and forms a sandwich structure (bacteria@apt@GO@MNPs) on the microcantilever surface, was stored in a refrigerator at 4 °C. The results showed that the reproducibility of the sensor (Fig. S9(a) in the ESM) was good, and the relative standard deviation (RSD) between groups was 3.07 %. Moreover, the microcantilever array can still detect obvious signals after 7 and 14 days, which proves that the stability of the sensor is good (Fig. S9(b) in the ESM). Moreover, in order to prove that our sensor has great potential in high-throughput detection, two different probes were modified on the microcantilever array to simultaneously detect two bacteria (*E. coli* and *S. aureus*). The detection results of Fig. 6(i) show that the sensor can simultaneously detect two kinds of bacteria at the concentrations of 10 CFU·mL^{-1}, and has high sensitivity.

Furthermore, to evaluate the detection capability of the GO-coupled MNPs method in actual samples, we simulated real samples with different bacterial concentrations by adding *E. coli* in milk. The detection process is illustrated in Fig. S10 in the ESM. The bacterial concentrations in milk were 100, 10, and 1 CFU·mL^{-1}. Except that the sample solution was milk, other experimental operations were consistent with the magnetic detection based on the MNP@GO@apt composite described previously. Different concentrations of *E. coli* produced differential deflections of 35, 14, and 6 nm in 4 mL milk samples, respectively (Figs. 6(g) and 6(h)). This result shows that the method can successfully detect 1

CFU·mL^{-1} of *E. coli* DH5*α* in milk samples without bacterial culture. Therefore, it indicates that our method has the ability to detect pathogenic bacteria in complex samples, which has great application potential in the field of food safety prevention and control.

In summary, using the large surface area of GO, more MNPs are concentrated. Compared with the MNPs composite, the GO-coupled MNPs composite increases the magnetic force applied to a single bacterium. Thus, in the presence of an external magnet, a larger magneto-mechanical deflection of the microcantilever occurs. Moreover, due to the large specific surface area of GO, the coupling efficiency of the aptamer can be improved, and the ability to capture the target can be improved. In actual samples, we capture bacteria by GO-coupled MNPs and then enrich and purify the bacterial complex (bacteria@apt@GO@MNPs) under magnetic force. The main advantage of this method is that although the concentration of the target is extremely low, it can enrich many MNPs, and the magnetic force generated by MNPs causes a large deflection of the microcantilever. Compared with the standard assay (conventional PCR) released by the Food and Drug Administration, USA (FDA) (Table S2 in the ESM) [42], this method does not require amplification, and its sensitivity, detection time have apparent advantages. However, detecting extremely low concentrations of bacteria requires some time for enrichment and concentration, and biochemical reactions. This magneto-mechanical biosensor based on GO-coupled MNPs strategy could be extended to many other biometrics, such as the detection of nucleic acid, protein, exosomes, and small molecules. More importantly, this ultra-sensitive detection method has great application prospects in food safety and clinical applications. It could be applied to the clinical detection of extremely low concentrations of pathogenic bacteria infection in the blood, as well as the screening of whether the cell therapy drugs meet the aseptic requirements.

3 Conclusions

In this study, we proposed a method to increase the magnetic force by using the sheet structure of GO to coat MNPs, which provides a novel strategy for early monitoring of food safety, clinical diagnosis of pathogenic bacteria infection, and improving the sensitivity of the sensor. The feasibility of this method was verified by using *E. coli* as a model bacterium. The magnetic nanomechanical sensor based on GO-coupled MNPs significantly improved the detection sensitivity and enabled the detection of a single bacterial cell per milliliter. Since GO coated multiple MNPs, which makes the number of MNPs much larger than the number of bacteria, and the aptamer coupling efficiency on the surface of GO is very high, it effectively enhances the probability of capturing the bacteria, and even 1 CFU·mL^{-1} of bacteria can be captured. For *E. coli*, compared with the traditional surface stress mode, the detection sensitivity of the magnetic mode based on GO-coupled MNPs was improved by 6 orders of magnitude (1 CFU·mL^{-1}), and the magnetic mode based on MNPs was improved by 4 orders of magnitude (100 CFU·mL^{-1}). Meanwhile, our method can detect actual samples with a detection limit of 1 CFU·mL^{-1} (in milk). We further found that at extremely low bacterial concentrations, the position of the bacteria binding to the microcantilever affects the deflection caused by the magnetic force, and the magnetic force is greater when applied at the tip. Based on this, we applied the magnetic force on the tip of the microcantilever to achieve a larger deflection. At the same time, we demonstrated the good specificity and anti-interference performance of this method using *Staphylococcus aureus* and *Salmonella*. Furthermore, the sensor showed good reproducibility and stability, and can also detect single bacterial cells in actual samples (in milk). We also tested the sensor's potential for high-throughput detection, enabling the simultaneous detection of two types of bacteria. In addition, by changing the modified probe molecules, our method is expected to achieve highly sensitive detection of other targets such as DNA, small molecules, proteins, and viruses.

Electronic Supplementary Material: Supplementary material (all experimental details, including sensor principle, materials, instruments, synthesis processes, detection procedures, characterization methods, and simulation results) is available in the online version of this article at https://doi.org/10.26599/NR.2025.94907290.

Data availability

All data needed to support the conclusions in the paper are presented in the manuscript and/or the Electronic Supplementary Material. Additional data related to this paper may be requested from the corresponding author upon request.

Acknowledgements

Financial support from the National Natural Science Foundation of China (Nos. 12232017, 12222212, and 12072339) is gratefully acknowledged.

Declaration of competing interest

All the contributing authors report no conflict of interests in this work.

Author contribution statement

Z. H. Q.: Conceptualization, investigation, methodology, experimental design, validation, visualization, data curation, writing manuscript. K. N. M.: Investigation, experimental design, methodology, validation, writing manuscript. Y. W.: Investigation, methodology. T. H. Y.: Methodology. S. B. Z.: Formal analysis. Q. B. C.: Formal analysis, visualization. Y. C.: Validation, visualization. C. W.: Visualization. T. X. R.: Formal analysis. S. Q. W.: Supervision, funding acquisition, project administration, review & editing. Q. C. Z.: Conceptualization, supervision, funding acquisition, project administration, review & editing. All the authors have approved the final manuscript.

Informed consent

Not applicable.

Ethics statement

Not applicable.

Use of AI statement

None.

References

[1] Zhou, X.; Hu, Z. W.; Yang, D. T.; Xie, S. X.; Jiang, Z. J.; Niessner, R.; Haisch, C.; Zhou, H. B.; Sun, P. H. Bacteria detection: From powerful SERS to its advanced compatible techniques. *Adv. Sci.* **2020**, *7*, 2001739.

[2] World Health Organization. *Food Safety in South-East Asia*[Online]. https://www.who.int/southeastasia/health-topics/food-safety (accessed May 28, 2024).

[3] Sharif, M. K.; Javed, K.; Nasir, A. Foodborne illness: threats and control. In *Foodborne Diseases*. Holban, A. M.; Grumezescu, A. M., Eds.; Academic Press: New York, 2018; pp 501–523.

[4] Huang, C. R.; Kuo, C. J.; Huang, C. W.; Chen, Y. T.; Liu, B. Y.; Lee, C. T.; Chen, P. L.; Chang, W. T.; Chen, Y. W.; Lee, T. M. et al. Host CDK-1 and formin mediate microvillar effacement induced by enterohemorrhagic *Escherichia coli*. *Nat. Commun.* **2021**, *12*, 90.

[5] Effa, E. E.; Lassi, Z. S.; Critchley, J. A.; Garner, P.; Sinclair, D.; Olliaro, P. L.; Bhutta, Z. A. Fluoroquinolones for treating typhoid and paratyphoid fever (enteric fever). *Cochrane Database Syst. Rev.* **2011**, *2011*, CD004530.

[6] Zhang, K. F.; Chang, S.; Zhang, Q.; Bai, Y. S.; Wang, E. R.; Zhang, M. L.; Fu, Q.; Wei, L. L.; Yu, Y. L. Heavy metals in influent and effluent from 146 drinking water treatment plants across China: Occurrence, explanatory factors, probabilistic health risk, and removal efficiency. *J. Hazard. Mater.* **2023**, *450*, 131003.

[7] Lin-Gibson, S.; Lin, N. J.; Jackson, S.; Viswanathan, S.; Zylberberg, C.; Wolfrum, J.; Basu, S.; Roy, K.; Marshall, D.; McFarland, R. et al. Standards efforts and landscape for rapid microbial testing methodologies in regenerative medicine. *Cytotherapy* **2021**, *23*, 390–398.

[8] Roddie, C.; O'Reilly, M.; Dias Alves Pinto, J.; Vispute, K.; Lowdell, M. Manufacturing chimeric antigen receptor T cells: Issues and challenges. *Cytotherapy* **2019**, *21*, 327–340.

[9] Robb, K. P.; Fitzgerald, J. C.; Barry, F.; Viswanathan, S. Mesenchymal stromal cell therapy: Progress in manufacturing and assessments of potency. *Cytotherapy* **2019**, *21*, 289–306.

[10] Opota, O.; Croxatto, A.; Prod'hom, G.; Greub, G. Blood culture-based diagnosis of bacteraemia: State of the art. *Clin. Microbiol. Infect.* **2015**, *21*, 313–322.

[11] Thaler, D. S. Toward a microbial Neolithic revolution in buildings. *Microbiome* **2016**, *4*, 14.

[12] Castelli, M.; Sabaneyeva, E.; Lanzoni, O.; Lebedeva, N.; Floriano, A. M.; Gaiarsa, S.; Benken, K.; Modeo, L.; Bandi, C.; Potekhin, A. et al. Deianiraea, an extracellular bacterium associated with the ciliate Paramecium, suggests an alternative scenario for the evolution of Rickettsiales. *ISME J.* **2019**, *13*, 2280–2294.

[13] Gracias, K. S.; McKillip, J. L. A review of conventional detection and enumeration methods for pathogenic bacteria in food. *Can. J. Microbiol.* **2004**, *50*, 883–890.

[14] López-Campos, G.; Martínez-Suárez, J. V.; Aguado-Urda, M.; López-Alonso, V. Detection, identification, and analysis of foodborne pathogens. In *Microarray Detection and Characterization of Bacterial Foodborne Pathogens*. López-Campos, G.; Martínez-Suárez, J. V.; Aguado-Urda, M.; López-Alonso, V., Eds.; Springer: Boston, 2012; pp 13–32.

[15] Ranjbar, S.; Shahrokhian, S.; Nurmohammadi, F. Nanoporous gold as a suitable substrate for preparation of a new sensitive electrochemical aptasensor for detection of Salmonella typhimurium. *Sens. Actuators B: Chem.* **2018**, *255*, 1536–1544.

[16] Pankratov, D.; Bendixen, M.; Shipovskov, S.; Gosewinkel, U.; Ferapontova, E. E. Cellulase-linked immunomagnetic microbial assay on electrodes: Specific and sensitive detection of a single bacterial cell. *Anal. Chem.* **2020**, *92*, 12451–12459.

[17] Kim, M. J.; Park, J.; Kang, M.; Jeong, U.; Jeong, D.; Kang, N. G.; Hwang, S. J.; Youn, S. H.; Hwang, B. K.; Hyun, Y. et al. Bacteria detection and species identification at the single-cell level using super-resolution fluorescence imaging and AI analysis. *Biosens. Bioelectron.* **2023**, *240*, 115603.

[18] Zhang, J.; Lang, H. P.; Huber, F.; Bietsch, A.; Grange, W.; Certa, U.; McKendry, R.; Güntherodt, H. J.; Hegner, M.; Gerber, C. Rapid and label-free nanomechanical detection of biomarker transcripts in human RNA. *Nat. Nanotechnol.* **2006**, *1*, 214–220.

[19] Kasas, S.; Ruggeri, F. S.; Benadiba, C.; Maillard, C.; Stupar, P.; Tournu, H.; Dietler, G.; Longo, G. Detecting nanoscale vibrations as signature of life. *Proc. Natl. Acad. Sci. USA* **2015**, *112*, 378–381.

[20] Huber, F.; Hegner, M.; Gerber, C.; Güntherodt, H. J.; Lang, H. P. Label free analysis of transcription factors using microcantilever arrays. *Biosens. Bioelectron.* **2006**, *21*, 1599–1605.

[21] Etayash, H.; Khan, M. F.; Kaur, K.; Thundat, T. Microfluidic cantilever detects bacteria and measures their susceptibility to antibiotics in small confined volumes. *Nat. Commun.* **2016**, *7*, 12947.

[22] Huber, F.; Lang, H. P.; Glatz, K.; Rimoldi, D.; Meyer, E.; Gerber, C. Fast diagnostics of BRAF mutations in biopsies from malignant melanoma. *Nano Lett.* **2016**, *16*, 5373–5377.

[23] Hansen, K. M.; Thundat, T. Microcantilever biosensors. *Methods* **2005**, *37*, 57–64.

[24] Kasas, S.; Malovichko, A.; Villalba, M. I.; Vela, M. E.; Yantorno, O.; Willaert, R. G. Nanomotion detection-based rapid antibiotic susceptibility testing. *Antibiotics* **2021**, *10*, 287.

[25] Wang, Y.; Yan, T. H.; Mei, K. N.; Rao, D. P.; Wu, W. J.; Chen, Y.; Peng, Y. P.; Wang, J. Y.; Wu, S. Q.; Zhang, Q. C. Nanomechanical assay for ultrasensitive and rapid detection of SARS-CoV-2 based on peptide nucleic acid. *Nano Res.* **2023**, *16*, 1183–1195.

[26] Rao, D. P.; Mei, K. N.; Yan, T. H.; Wang, Y.; Wu, W. J.; Chen, Y.; Wang, J. Y.; Zhang, Q. C.; Wu, S. Q. Nanomechanical sensor for rapid and ultrasensitive detection of tumor markers in serum using nanobody. *Nano Res.* **2022**, *15*, 1003–1012.

[27] Li, C.; Zhang, G. P.; Wu, S. Q.; Zhang, Q. C. Aptamer-based microcantilever-array biosensor for profenofos detection. *Anal. Chim. Acta* **2018**, *1020*, 116–122.

[28] Wang, J. H.; McIvor, M. J.; Elliott, C. T.; Karoonuthaisiri, N.; Segatori, L.; Biswal, S. L. Rapid detection of pathogenic bacteria and screening of phage-derived peptides using microcantilevers. *Anal. Chem.* **2014**, *86*, 1671–1678.

[29] Nugaeva, N.; Gfeller, K. Y.; Backmann, N.; Lang, H. P.; Düggelin, M.; Hegner, M. Micromechanical cantilever array sensors for selective fungal immobilization and fast growth detection. *Biosens. Bioelectron.* **2005**, *21*, 849–856.

[30] Gil-Santos, E.; Ramos, D.; Jana, A.; Calleja, M.; Raman, A.; Tamayo, J. Mass sensing based on deterministic and stochastic responses of elastically coupled nanocantilevers. *Nano Lett.* **2009**, *9*, 4122–4127.

[31] Kosaka, P. M.; Pini, V.; Ruz, J. J.; da Silva, R. A.; González, M. U.; Ramos, D.; Calleja, M.; Tamayo, J. Detection of cancer biomarkers in serum using a hybrid mechanical and optoplasmonic nanosensor. *Nat. Nanotechnol.* **2014**, *9*, 1047–1053.

[32] Sungkanak, U.; Sappat, A.; Wisitsoraat, A.; Promptmas, C.; Tuantranont, A. Ultrasensitive detection of *Vibrio cholerae* O1 using microcantilever-based biosensor with dynamic force microscopy. *Biosens. Bioelectron.* **2010**, *26*, 784–789.

[33] Mei, K. N.; Yan, T. H.; Wang, Y.; Rao, D. P.; Peng, Y. P.; Wu, W. J.; Chen, Y.; Ren, M.; Yang, J.; Wu, S. Q. et al. Magneto-nanomechanical array biosensor for ultrasensitive detection of oncogenic exosomes for early diagnosis of cancers. *Small* **2023**, *19*, e2205445.

[34] Rao, D. P.; Yan, T. H.; Qiao, Z. H.; Wang, Y.; Peng, Y. P.; Tu, H.; Wu, S. Q.; Zhang, Q. C. Relay-type sensing mode: A strategy to push the limit on nanomechanical sensor sensitivity based on the magneto lever. *Nano Res.* **2023**, *16*, 3231–3239.

[35] Patil, P. O.; Pandey, G. R.; Patil, A. G.; Borse, V. B.; Deshmukh, P.

K.; Patil, D. R.; Tade, R. S.; Nangare, S. N.; Khan, Z. G.; Patil, A. M. et al. Graphene-based nanocomposites for sensitivity enhancement of surface plasmon resonance sensor for biological and chemical sensing: A review. *Biosens. Bioelectron.* **2019**, *139*, 111324.

[36] Wang, Y.; Li, S. S.; Yang, H. Y.; Luo, J. Progress in the functional modification of graphene/graphene oxide: A review. *RSC Adv.* **2020**, *10*, 15328–15345.

[37] Zhang, Z.; Zhang, J.; Zhang, B. L.; Tang, J. L. Mussel-inspired functionalization of graphene for synthesizing Ag-polydopamine-graphenenanosheets as antibacterial materials. *Nanoscale* **2013**, *5*, 118–123.

[38] Tian, B.; Han, Y. Y.; Fock, J.; Strömberg, M.; Leifer, K.; Hansen, M. F. Self-assembled magnetic nanoparticle-graphene oxide nanotag for optomagnetic detection of DNA. *ACS Appl. Nano Mater.* **2019**, *2*, 1683–1690.

[39] Pham, X. H.; Hahm, E.; Kim, H. M.; Son, B. S.; Jo, A.; An, J.; Tran Thi, T. A.; Nguyen, D. Q.; Jun, B. H. Silica-coated magnetic iron oxide nanoparticles grafted onto graphene oxide for protein isolation. *Nanomaterials* **2020**, *10*, 117.

[40] Nolte, H.; Schilde, C.; Kwade, A. Determination of particle size distributions and the degree of dispersion in nanocomposites. *Compos. Sci. Technol.* **2012**, *72*, 948–958.

[41] Akbarzadeh, A.; Samiei, M.; Davaran, S. Magnetic nanoparticles: Preparation, physical properties, and applications in biomedicine. *Nanoscale Res. Lett.* **2012**, *7*, 144.

[42] Kang, D. K.; Ali, M. M.; Zhang, K. X.; Huang, S. S.; Peterson, E.; Digman, M. A.; Gratton, E.; Zhao, W. A. Rapid detection of single bacteria in unprocessed blood using Integrated Comprehensive Droplet Digital Detection. *Nat. Commun.* **2014**, *5*, 5427.